

Chapter 10

Geometric Diodes for Optical Rectennas

Zixu Zhu, Saamil Joshi, Sachit Grover, and Garret Moddel

Abstract A new diode called a geometric diode rectifies based on geometric asymmetry of a conducting thin film. The planar structure of the geometric diode provides a low RC time constant (on the order of 10^{-15} s) that is required for rectenna operation at optical frequencies and a low impedance for efficient power transfer from the antenna. Fabricated graphene geometric diodes show asymmetric DC current–voltage characteristics consistent with Monte Carlo simulations for the devices. Coupled to an antenna to form a rectenna, we demonstrated rectification for 28 THz radiation. The geometric diode rectenna system detectivity is in theory 10 times higher than for a metal–insulator–metal diode operating at 28 THz. Applications for this diode include terahertz-wave and optical detection, ultrahigh speed electronics, and optical power conversion.

10.1 Introduction

The most widely used diode in terahertz rectenna research is the metal–insulator–metal (MIM) diode, which is limited in frequency response because of fundamental RC constraints in parallel plate devices [1], as described in Chap. 5. One challenge of harvesting solar energy using rectennas is finding diodes and antennas that respond efficiently at petahertz optical frequencies. The diode must provide low resistance (R) while simultaneously providing low capacitance (C). The low R is needed to couple power efficiently from the antenna, which generally has a low impedance, and the low

Z. Zhu (✉) • S. Joshi • G. Moddel
Department of Electrical, Computer, and Energy Engineering,
University of Colorado, 425 CUB, Boulder, CO 80309-0425, USA
e-mail: zixu.zhu@colorado.edu

S. Grover
National Center for Photovoltaics, National Renewable Energy Laboratory,
15013 Denver West Parkway, Golden, CO 80309-0425, USA

C is needed for a sufficiently small RC time constant to respond to optical frequencies. The RC cannot be reduced by reducing device area for MIM diodes because with decreasing area the C decreases but the R increases proportionately [1]. Even with ideal materials, lumped-element parallel-plate MIM diodes cannot simultaneously achieve the required combination of low R and low C [1]. We propose and demonstrate a new type of diode, called a geometric diode, which, because of its planar structure, does not suffer from the RC constraints of parallel plate devices. Because it is formed from a conductive material, the resistance of the geometric diode is also sufficiently low to match the antenna impedance [2]. The results given in this chapter are an elaboration of recently published work [1–5].

10.2 Background

The geometric diode is a ballistic transport device [6] using long mean-free path length (MFPL) material with physical asymmetry that determines the preferred direction of the charge movement. The device consists of a patterned conductive thin film in which the size of the constriction is on the order of the MFPL of the charge carriers in the material. When the constriction length of the device is on this scale, the motion of charge carriers can be considered ballistic, such that the boundaries and the geometry of the device have a substantial impact on the charge movement [6]. Ballistic devices depending on the geometric shape to provide electric rectification have also been demonstrated from other groups. Song demonstrated semiconductor devices that act as a full wave rectifier due to their geometric asymmetry [7].

10.3 Principle of Operation

The boundaries and the shape of the geometric diode have substantial impact on charge movement. In Fig. 10.1, we show the top view of a geometric diode. The critical region of the device is the inverse arrowhead-shaped constriction (neck).

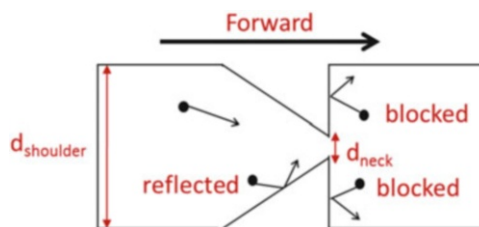


Fig. 10.1 Inverse arrowhead geometric diode structure. The neck width (d_{neck}) is on the order of the mean-free path length (MFPL) of the charge carriers in the material. The forward direction of this arrowhead diode is from left to right. The charge carriers reflect at the boundaries of the device. On the left side of the neck charge carriers can either channel directly through the neck region or reflect at the tapering edge and keep moving forward. On the right side of the neck the vertical edge blocks most of the electrons

The width of the neck (d_{neck}) is on the order of the MFPL so that the boundaries of the device can affect the charge movement. Due to the inverse arrowhead shape and the neck constriction, charge carriers move more freely in the forward direction (left to right in Fig. 10.1) than in the reverse direction. The carriers have higher probability of channeling through the arrowhead region on the left side of the neck and are likely to be blocked at the flat walls on the right side of the arrowhead. The asymmetric probabilities in the electron net flow directions cause dissimilar current levels for forward- and reverse-biased voltages.

10.4 Material Choices

10.4.1 Metal

The geometric diode material has to meet two requirements. The first is electrical reliability at a high current density of up to 10^7 A/cm². This estimation is calculated based on the required voltage drop across the device from the simulation result that will be shown in Fig. 10.8. The second is that the charge carrier MFPL of the material has to be relatively long so that the physical shape of the diode can influence the charge carrier movement and allow for devices that are sufficiently large and within the capabilities of current lithographic fabrication techniques.

We chose metal as the first and easiest option because it is easy to deposit as a planar conductive thin film. The MFPL in metals at room temperature is 10–30 nm [8], which requires extremely fine nanoscale patterning to make a geometric diode. Further, the MFPL of thermally deposited thin film metals is limited by the grain size of the metal particles shown in Fig. 10.2. Therefore, the actual MFPL of the thin film metal could be below 10 nm, since the conduction of the device is limited by the electron reflections at the grain boundaries [9] rather than at the boundaries of the thin film.

In addition to the grain boundary limitation, thin film metal structures with a small junction area suffer from electromigration. We fabricated a 100 nm wide neck geometric diode using silver, patterned using focused ion beam (FIB) lithography,

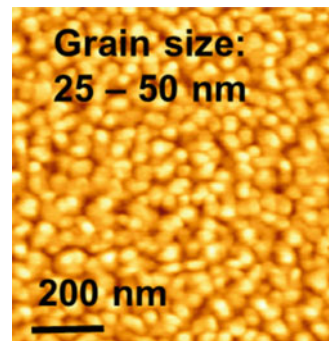


Fig. 10.2 Atomic force microscope (AFM) image of grains in a gold film that is 30 nm thick. The grain size is 25–50 nm

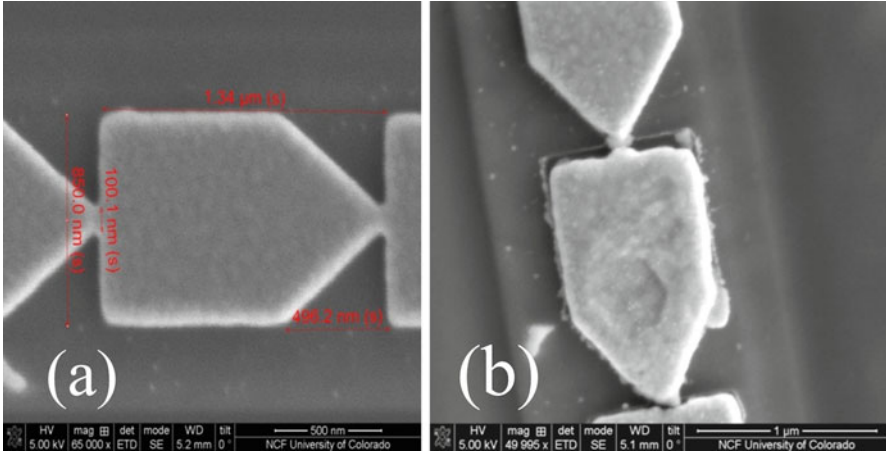


Fig. 10.3 (a) Fifty nanometer thick silver geometric diode fabricated using focused ion beam (FIB) patterning. The achieved neck width is 100 nm. (b) After the DC $I(V)$ measurement, electromigration physically shifted the silver structure and formed an open circuit

as shown in Fig. 10.3a. Figure 10.3b shows that after the DC current–voltage [$I(V)$] measurement was taken, electromigration physically shifted the device and made it nonconductive.

10.4.2 Graphene

Because of the size and reliability limitations of metal, graphene may be a better choice for making geometric diodes. The MFPL in graphene can be as long as 1 μm with carrier mobility as high as 200,000 $\text{cm}^2/\text{V s}$ [10]. Graphene is also able to carry a current density up to $10^8 \text{ A}/\text{cm}^2$ [11], and the conical band structure of graphene allows the carrier concentration to be modulated by an electrically insulated gate [12]. Details of this gate effect measurement and the quality of our graphene will be described in Sect. 10.6.

10.5 Fabrication of Geometric Diode

The graphene geometric diodes were fabricated with a four-point probe configuration to remove the contact resistance from the measurement. We used exfoliation to produce graphene flakes on 90 nm thermally grown SiO_2 silicon wafer substrates. Four metal contacts (15 nm Cr/40 nm Au) were thermally evaporated and lifted off using resist patterned by photolithography. In Fig. 10.4, we show the process steps for patterning the graphene geometric diode using

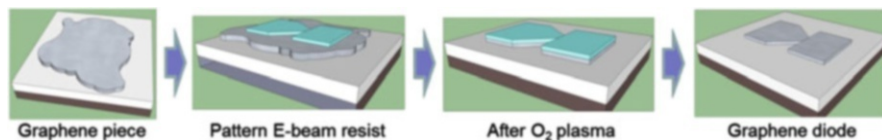


Fig. 10.4 Fabrication process flow of graphene geometric diode

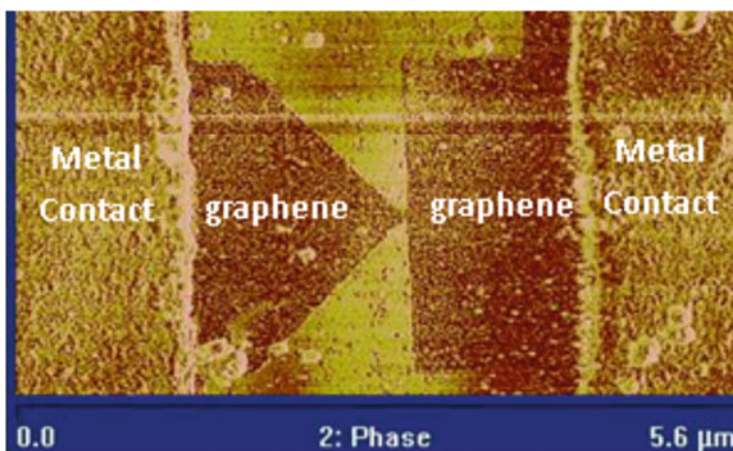


Fig. 10.5 AFM image of a graphene geometric diode placed between two metal contacts. The measured neck size is 75 nm. The graphene looks grainy in the figure because its roughness follows the roughness of the SiO₂ substrate, which is on the order of 1–10 nm

electron-beam (e-beam) lithography followed by an oxygen plasma etch. We used maN negative resist and a JEOL 9300 electron beam writer for the e-beam patterning process. An Oxford PlasmaLab 80+ RIE system with an oxygen plasma power of 50 W was used for 12 s to etch the graphene. The achieved neck size is approximately 75 nm measured from the atomic force microscope (AFM) image shown in Fig. 10.5 [4].

10.6 DC $I(V)$ Characteristics

The four-point probe configuration is shown in Fig. 10.6. DC $I(V)$ measurements were performed by measuring the voltage drop between the inner contacts while passing a current through the outer contacts of a geometric diode. A DC gate voltage was applied to the silicon substrate to control the majority charge carrier concentration in the graphene. A Keithley 2612 SourceMeter set to the four-wire mode applied a pulsed voltage to the outer contacts. The voltage was pulsed to prevent heating the graphene and avoid hysteresis that results from charge buildup [13]. The pulse width was 23 μs, followed by a 5-s relaxation time. The absolute

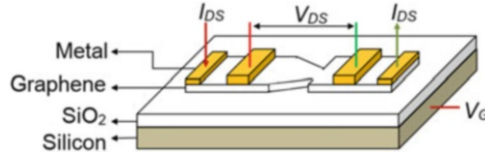


Fig. 10.6 Four-point probe setup to eliminate contact resistance from the measurement. The drain-source current (I_{DS}) is passed through the outer metal contacts, and the voltage drop across the diode (V_{DS}) is measured between the inner metal contacts. The gate voltage (V_G) is applied directly to the silicon substrate

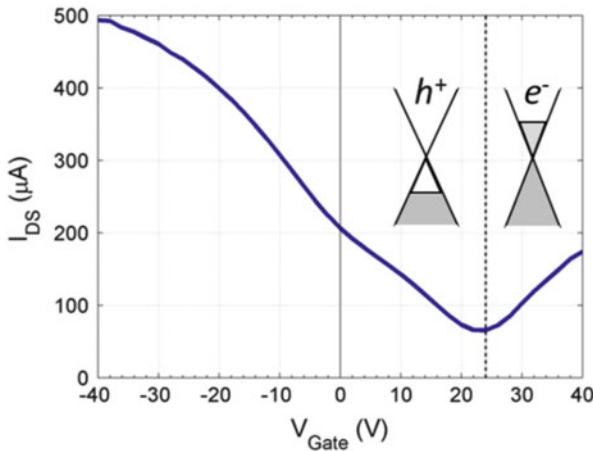


Fig. 10.7 Dirac curve [drain-source current (I_{DS}) vs. gate voltage (V_G)] of a graphene geometric diode at drain-source voltage $V_{DS} = 1.5$ V. The charge neutral point voltage (V_{CNP}) is at 24 V. The band diagram on two sides of V_{CNP} is shown in the figure. The grey area of the band diagram represents the occupation of electrons below Fermi level. The majority charge carriers are holes when V_{Gate} is less than V_{CNP} and become electrons at $V_{Gate} > V_{CNP}$

value of the voltage was stepped from 0 V to V_{end} , and the polarity continuously switched following the pattern: 0 V, V_i , $-V_i$, V_{i+1} , $-V_{i+1}$, \dots , V_{end} , $-V_{end}$.

Using the setup in Fig. 10.6, the MFPL can be calculated from a measurement of the drain-source current (I_{DS}) vs. gate voltage (V_G), sometimes called the Dirac curve. Figure 10.7 shows the conic Dirac curve [12] of a graphene piece after device fabrication. In the graphene Dirac curve, there is a gate voltage (V_G), at which the device has a minimum drain-source current (I_{DS}). This V_G is called charge neutral point (CNP) voltage (V_{CNP}), where the electron (e^-) and hole (h^+) have the same lowest density and conductivity of graphene reduces to a minimum. The graphene in Fig. 10.7 has a V_{CNP} of 24 V. The CNP separates the Dirac curve into two regions. When V_G is below V_{CNP} , holes are the majority charge carriers. Otherwise, if V_G is greater than V_{CNP} , electrons are the majority charge carriers. In both cases, when V_G moves further away from V_{CNP} , the concentration and the MFPL of the

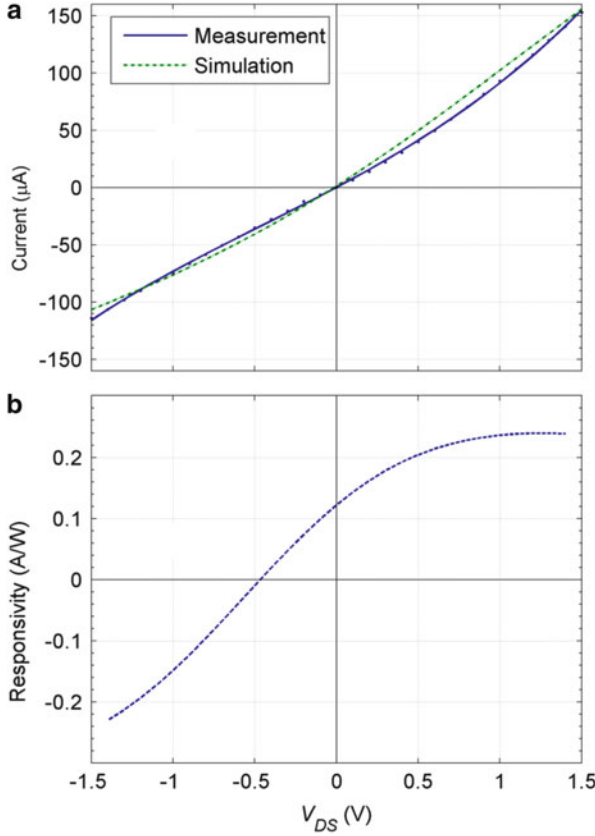


Fig. 10.8 (a) DC $I(V)$ characteristics for an exfoliated graphene geometric diode at $V_G = 20$ V. The Monte Carlo simulation used the dimensions of the fabricated device: neck width = 75 nm, shoulder width = 400 nm, and the measured MFPL = 50 nm. Details of the simulation will be discussed in Sect. 10.9. (b) Calculated responsivity $[1/2I''(V)/|I'(V)|]$ using measurement data as a function of the applied bias. At 0 V bias, the responsivity is 0.12 A/W

majority charge carriers increase and contribute to the increase of I_{DS} under the same drain-source voltage (V_{DS}) [12]. From the Dirac curve, we estimate that the MFPL of our graphene piece is approximately 45 nm [12].

Figure 10.8a shows the measured $I(V)$ curve of an exfoliated graphene diode. It exhibits a significant asymmetry in a direction that is consistent with the geometric asymmetry, and the measured characteristics are consistent with simulation described in Sect. 10.9. Using the $I(V)$ measurement data in Fig. 10.8a, the responsivity of the graphene geometric diode at zero bias was calculated to be 0.12 A/W, as shown in Fig. 10.8b. The diode responsivity is an important factor when considering its operation as a rectenna [1]. Responsivity is defined as half the ratio of the second and first derivative of the $I(V)$ characteristic. It is a measure of the rectified DC current out divided by the AC power in.

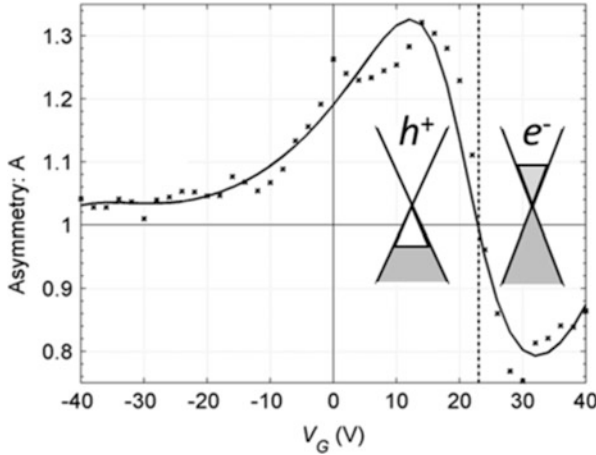


Fig. 10.9 Calculated asymmetry ($A = I(V_{DS})/I(-V_{DS})$) as a function of gate voltage. The *dotted line* is the measured data and the *solid line* is a fit to the measurement result. The direction of diode asymmetry switches as the gate voltage is varied from -40 to 40 V. This is due to the change of the charge carrier type from holes (h^+) to electrons (e^-) near V_{CNP} ($=24$ V). A current saturation effect starts playing a major role after the diode asymmetry ratio reaches its maximum as $|V_G - V_{CNP}|$ increases

To confirm that the geometric effect of the diode is consistent with the majority carriers in graphene, we varied the V_G at fixed V_{DS} . Because the forward direction in geometric diodes depends only on the geometry and is independent of carrier type, applying a gate voltage to change the majority charge carrier type should reverse the polarity of the diode. This is, in fact, the case [4] and it serves as confirmation that the rectification is due to the geometry. We define diode asymmetry A to be equal to $|I(V_{DS})/I(-V_{DS})|$. In Fig. 10.9 A is shown as a function of V_G for a fixed V_{DS} . For $A > 1$ the current flows more easily in the arrowhead pointing direction, while for $A < 1$ the current flows more easily in the opposite direction. Figure 10.9 shows that the polarization of the diode can be controlled experimentally by varying V_G . By increasing the voltage difference between V_G and V_{CNP} ($|V_G - V_{CNP}|$), the charge carrier concentration n_s increases and gives longer MFPL ($\propto \sqrt{n_s}$) [12]. This causes A to move away from unity in the region of $V_G = 12\text{--}24$ and $24\text{--}32$ V. As $|V_G - V_{CNP}|$ keeps increasing the graphene current saturation [14] starts affecting the $I(V)$ characteristic and A drops back to unity [4].

We compare the asymmetry shown by the exfoliated graphene diode to that of a geometric diode made with graphene deposited using chemical vapor deposition (CVD). The CVD graphene (provided by P.L. McEuen's lab at Cornell University) had a shorter MFPL than that of the exfoliated graphene due to the impurity doping during the CVD process and the small grain size of CVD graphene. As shown in Fig. 10.10, devices made from CVD graphene, having the same dimensions as

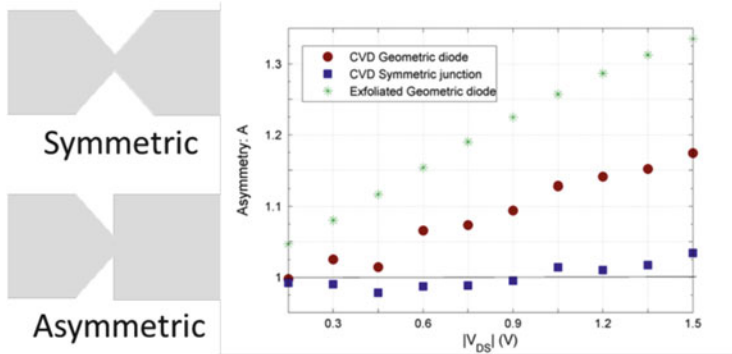


Fig. 10.10 Current–voltage asymmetry A vs. drain-source voltage V_{DS} characteristics of chemical vapor deposition (CVD) graphene geometric diode (*red*) and exfoliated graphene geometric diode (*green*). The *blue baseline* is A of the symmetric junction device ($A = 1$). CVD graphene has a shorter MFPL than the exfoliated graphene and gives a diode a lower asymmetry than the exfoliated graphene device

devices made from exfoliated graphene, exhibit a lower asymmetry. As a control, we also fabricated a symmetric junction, which as expected, does not show any asymmetry in its $I(V)$ curve.

10.7 Rectification at 28 THz

We designed and fabricated a rectenna using the graphene geometric diode to measure its rectification response at 28 THz. The rectenna consists of a $5.1 \mu\text{m}$ long metal bowtie antenna and a 500 nm long geometric diode at the center, as shown in Fig. 10.11a. The bowtie antenna (in the edge-fed configuration [15]) is a combination of two opposing $2.3 \mu\text{m}$ triangular sections with a 500 nm gap [16].

In Fig. 10.12, we show the measurement setup. A $10.6 \mu\text{m}$ wavelength infrared (IR) laser was used as the source of radiation. The intensity of the CO_2 laser was controlled by a pulse generator. A half wave plate was used to change the polarization of the incoming beam relative to the antenna axis. We used a He–Ne laser to align the CO_2 laser with the device. A mercury switch was used to keep the probes at ground potential when not in use, to avoid damaging the devices due to stray charges.

Zero-bias current and open-circuit voltage, generated by shining the IR laser on the rectenna, were measured using a lock-in amplifier (Stanford Research Systems SR830). The laser beam was chopped at a reference frequency 280 Hz thereby modulating the current and the voltage at that frequency. There was no V_G applied, because A is sufficient at $V_G = 0 \text{ V}$ as seen from Fig 10.9. Figure 10.13 shows the zero-bias current and the open-circuit voltage measured at different polarization angles of the beam, relative to the metal antenna/graphene geometric diode

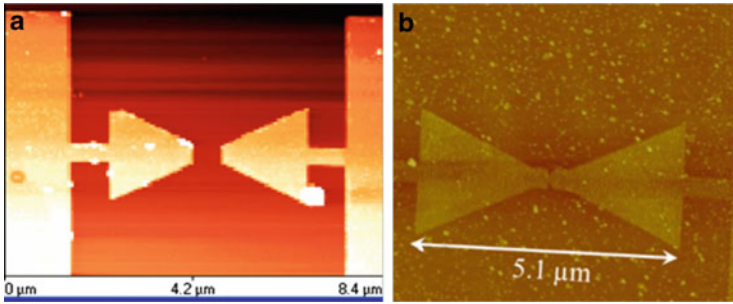


Fig. 10.11 AFM image of the bowtie antenna coupled to a geometric diode: (a) the metal antenna/graphene geometric diode. The difference in the thickness of the metal and graphene layers gives rise to a contrast that leaves the graphene indistinguishable in (a). (b) The graphene antenna/graphene geometric diode rectenna device

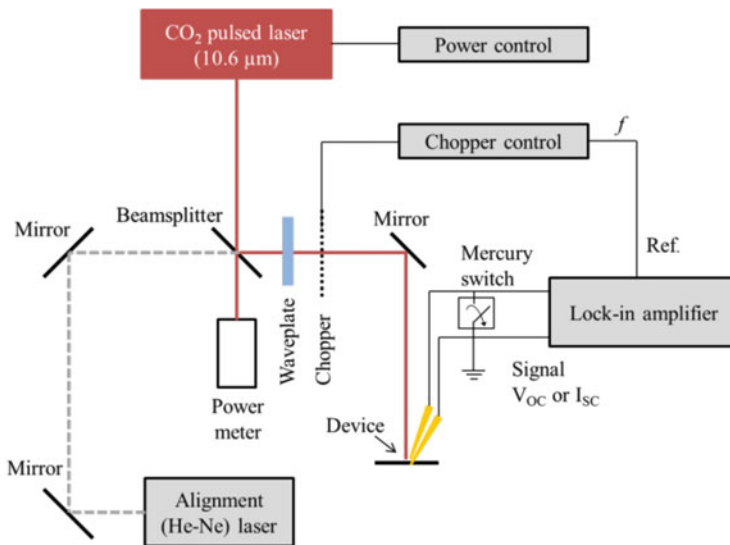


Fig. 10.12 Setup for measuring the optical response of rectennas. The CO_2 laser beam is chopped at a frequency of 280 Hz and guided to the device using a set of mirrors and a red laser for beam alignment. A wave plate is used to study the effect of the change in the angle of polarization between the antenna axis and the incident wave. A lock-in amplifier and a two-point probe setup are used to measure the photocurrent, with the chopping frequency used as a reference

rectenna system. The cosine-squared characteristics confirm the optical response of the bowtie antenna. We have also fabricated a graphene antenna/graphene geometric diode rectenna system, as shown in Fig. 10.11b. Its optical response in Fig. 10.14 displays the same cosine-squared characteristics as the response of the metal antenna rectenna system. The open-circuit voltage response is similar to that of the graphene diode/metal antenna rectenna. The lower current response is due to

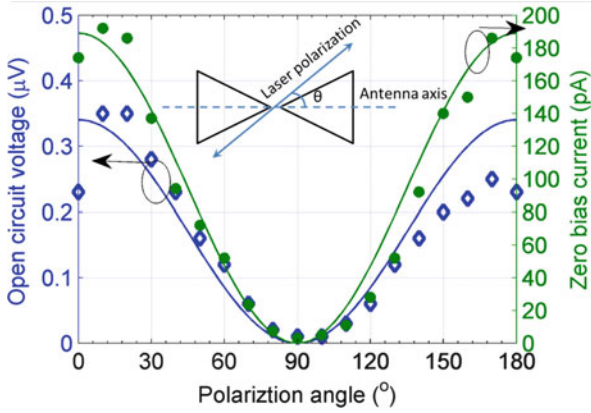


Fig. 10.13 Metal antenna/graphene diode rectenna zero-bias current (green circle) and open-circuit voltage (blue diamond) as a function of polarization angle (θ)

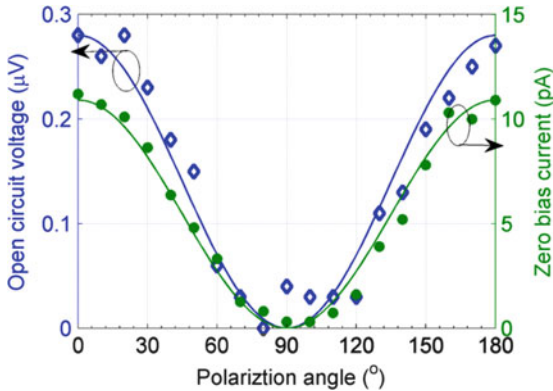


Fig. 10.14 Graphene antenna/graphene diode rectenna zero-bias current (green circle) and open-circuit voltage (blue diamond) response at different polarization angles. The lower current response in the graphene rectenna is due to a larger series resistance than the metal antenna

the much larger series resistance, which is about 1 kΩ for the graphene antenna comparing to a few ohms for the metal antenna.

Figure 10.15 shows the rectified voltage with increasing incident power on the rectenna system, at two polarization angles (180° and 90°) of the metal antenna relative to the incident wave. The voltage signal increases with increasing incident power when the antenna is aligned (180°) with the polarization of the laser, while there was no change of voltage the in the fully misaligned (90°) case, again confirming that the measured output is due to incident radiation coupled through the antenna.

The angular dependence of the response indicates that rectification was not a result of optically generated charge diffusion nor a result of thermoelectric effects

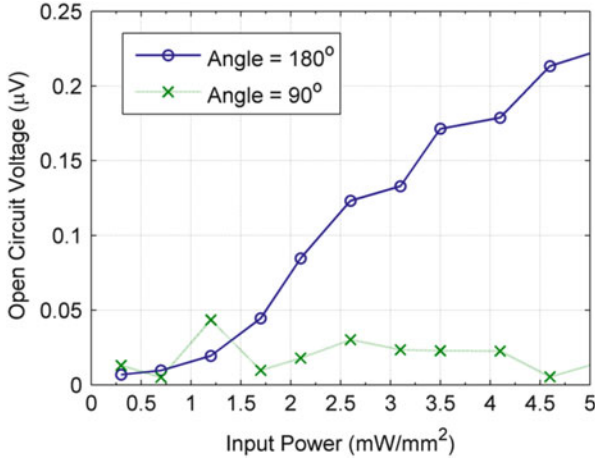


Fig. 10.15 Open-circuit voltage vs. laser input power. The response at 180° (blue circle) indicates perfect alignment between the laser polarization and the antenna, which gives the strongest open-circuit voltage signal. At 90° (green cross), the antenna is perpendicular to the laser polarization and gives a near-zero output voltage

due to a difference in the illumination of the two sides of the junction. Additionally, no response was detected from an illuminated diode that was not coupled to an antenna showing that the optical response is not caused by an in situ p–n doping in the graphene. Furthermore, since no gate voltage was applied to the antenna-coupled diodes before or during the measurement, no p–n junctions could have been formed as a result of an applied field [17]. The geometric diode genuinely responds to and rectifies 28 THz signals.

We compared the measured maximum current of 190 pA of the metal antenna/graphene diode rectenna to the expected current through the following steps. Based on the measured laser beam power and beam width, we estimated an input intensity of 5.6 mW/mm [2] over an antenna area of approximately $37.5 \mu\text{m}^2$ [16]. The diode/antenna coupling efficiency is calculated to be 12 % [1, 18] for a 3,000 Ω diode and an antenna with a characteristic impedance of 100 Ω , and the antenna radiation efficiency is estimated to be 37 % [16]. Although the bowtie antenna efficiency was poor, we chose it because of its relative ease of fabrication. The zero-bias DC responsivity of the diode used in this optical measurement was measured to be 0.0285 A/W. Combining the estimated antenna parameters with the input power and the diode responsivity gives an estimated current of 270 pA, which is close to the measured value of 190 pA. A current of 190 pA for a 10.6 μm wavelength corresponds to a quantum efficiency of 0.01 %. Design improvements are expected to improve the antenna and diode efficiencies. A similar but smaller geometric diode (50 nm shoulder width with 10 nm neck width) has been simulated to have more nonlinear and asymmetric $I(V)$ characteristics than reported here [19].

10.8 Frequency Limitation Based on RC Time Constant Estimation

The RC time constant of the geometric diode is estimated to be on the order of 10^{-15} s, which is small enough for the diode to work at optical frequencies. To calculate the capacitance we look at the two possible locations which can store charges through the electric fringing fields. The first electric fringing field locates between the two sides of the geometric diode through the air above the device. The second electric fringing field goes through the 90 nm SiO_2 bottom substrate underneath the diode. To estimate the worst-case capacitance between the two sides of the neck, we assume that there is an approximately 100 nm by 100 nm air gap at the neck region. Using the planar thin film capacitance analysis method [20], the capacitance of a graphene geometric diode is calculated to be a few attofarads. The measured resistance of the graphene device is approximately 1 k Ω , which gives an overall RC time constant on the scale of femtoseconds, corresponding to a cutoff frequency of 100 THz. By reducing the area of the noncritical region around the neck, the RC time constant can be reduced further.

10.9 Geometric Diode Simulation

10.9.1 Monte Carlo Simulation Based on Drude Model

The $I(V)$ asymmetry of the diode was modeled using a Monte Carlo simulation based on the Drude model [8]. In the simulation, an electron is positioned randomly in the device and set into random motion until it collides with defects or phonons. Elastic scattering is assumed to occur during collision [12]. In between collisions, the electron is set to maintain a velocity (v_{tot}), which is a combination of the random Fermi velocity (v_F) and the constant drift velocity (v_D) due to a bias-dependent electric field. The electric field is assumed to be uniform within the device so that v_D is constant at a fixed bias voltage. The electron specularly reflects at the boundaries of the diode and its motion is tracked until 10^6 collisions have occurred. The final current is calculated by counting the number of times an electron crosses a certain device cross section per unit of time. Carrying out the scattering process for a large collision count ensures a statistically stable result, which is independent of the starting position.

The size of the neck and the device's geometric asymmetry determines the $I(V)$ asymmetry. We vary these parameters and simulate the $I(V)$ curves of the resulting device geometries using the Monte Carlo method described above. Figure 10.16a indicates that shrinking the neck size while keeping all other device dimensions the same increases the $I(V)$ asymmetry. The MFPL is the key material parameter used in the simulation, which we assumed to be 200 nm for graphene. Using the $I(V)$ data of Fig. 10.16a, the asymmetry ratio is plotted in

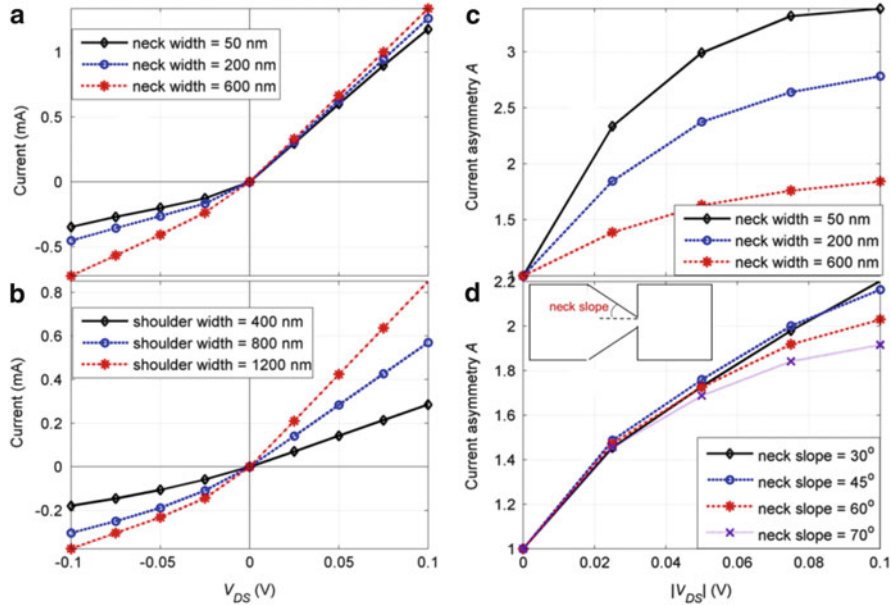


Fig. 10.16 Monte Carlo simulation results. (a) Simulated $I(V)$ curves of the geometric diode with different neck widths: 50, 200, and 600 nm. The shoulder width is fixed at 1 μm . The neck width has strong effect on the diode reverse current. A smaller neck restricts the reverse current more efficiently. (b) Simulated $I(V)$ curves of geometric diode with different shoulder widths: 400, 800, and 1,200 nm. The neck width is fixed at 50 nm. Wider shoulders increase the forward current more than the reverse current. (c) Calculated asymmetry A vs. neck width using the data from (a). Increasing V_{DS} and reducing neck width leads to higher asymmetry. (d) Calculated asymmetry A vs. arrowhead neck slope varying from 30° to 70°. Within this range, the slope angles do not have a great impact on A . The MFPL in all the simulations is fixed to be 200 nm

Fig. 10.16c as a function of V_{DS} for different neck sizes. The plot shows that increasing V_{DS} and reducing neck size leads to higher asymmetry. However, A saturates at high V_{DS} because a large electric field makes the electrons move a distance far greater than d_{neck} during one collision time. The sloped boundaries start to block the electron movement as effectively as the vertical boundaries. Electrons have equal possibility to funnel through the neck region from both sides and their flow becomes insensitive to the physical structure.

The shoulder size and the neck slope of the arrowhead are the other two limiting factors of A . Figure 10.16b shows $I(V)$ plots for varying shoulder size. The size of shoulder determines the ease of electron movement once it passes through the critical neck region. Increasing the shoulder size gives a higher forward current. As for the diode neck slope, between 30° and 70° the neck slope does not have a strong effect on A , as shown in Fig. 10.16d.

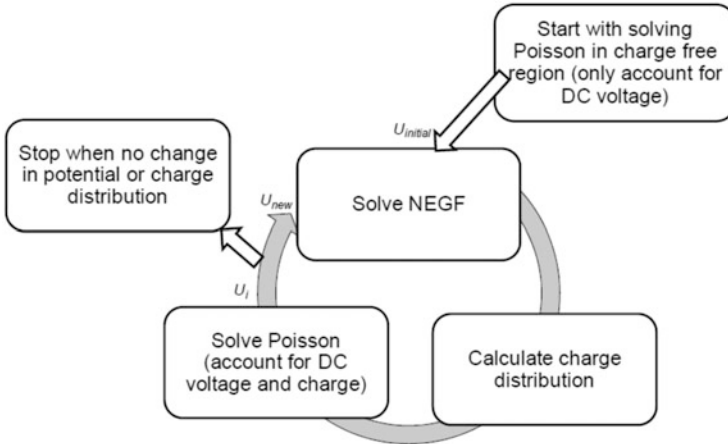


Fig. 10.17 Flowchart of the quantum simulation. The simulation starts from the initial potential map calculated using Poisson’s equation, assuming DC voltage and no charge interaction. Nonequilibrium Green’s function (NEGF) solver calculates the charge distribution based on the initial potential map and passes the result to Poisson solver to get the updated potential map, which is sent back to the NEGF solver. The loop keeps running until the potential and the charge distribution converge to a self-consistent solution

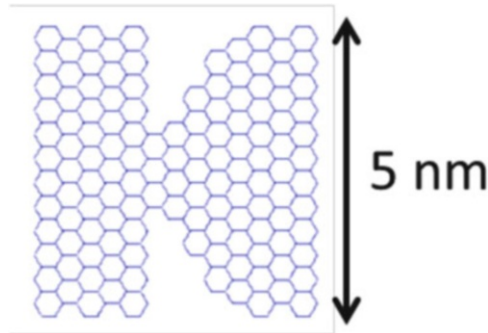


Fig. 10.18 The atomic structure of the graphene device used in the quantum simulation

10.9.2 Quantum Simulation

In this section we describe quantum mechanical simulations used to obtain the DC $I(V)$ characteristics of geometric diodes [5]. This requires the simultaneous solution of the Poisson’s equation and the nonequilibrium Green’s function (NEGF) [21, 22] to find a self-consistent device potential profile and charge distribution. Figure 10.17 outlines the logical flow of the NEGF-Poisson solver used in the quantum simulation. Due to the computational complexity of the method, we simulated a relatively small device geometry confined to an area of 5 nm by 5 nm. As shown in Fig. 10.18, only a few atoms make up the 1.5 nm neck. In Fig. 10.19

Fig. 10.19 Asymmetric $I(V)$ characteristics of the geometric diode shown in Fig. 10.18

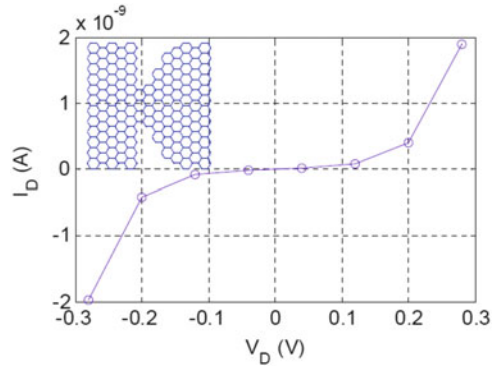
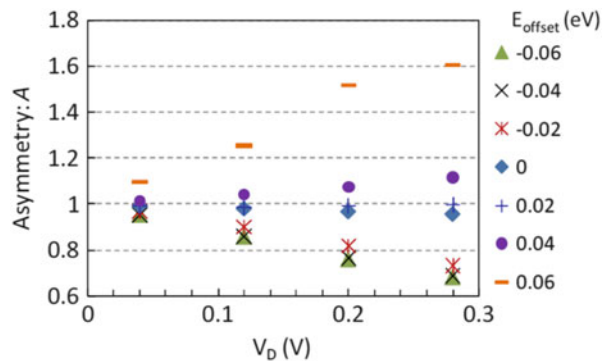


Fig. 10.20 Forward-to-reverse current asymmetry ($A = I(V_{DS})/I(-V_{DS})$) vs. drain-source voltage (V_{DS}) with changing E_{offset} . When E_{offset} is positive, the graphene is p-type and $A < 1$. When E_{offset} is negative, the graphene is n-type and $A > 1$. The device structure and size is shown in Fig. 10.18



we show the $I(V)$ curves generated from quantum simulation of the geometric diode in Fig. 10.18.

The quantum simulation can also simulate the effect of gate on a graphene device by changing the Bloch energy at each graphene atom by an energy amount of E_{offset} [23, 24]. This change is equivalent to changing the Fermi level of the graphene. For $E_{\text{offset}} > 0$ eV, the graphene is p-type, while for $E_{\text{offset}} < 0$ eV, the graphene is n-type. By plotting A vs. V_{DS} under different E_{offset} , the quantum simulation results in Fig. 10.20 also shows the reversible diode behavior, which is confirmed by the measurement result in Fig. 10.9.

10.10 Infrared Detection: Comparison with MIM Technology

To compare the geometric diode rectenna with other detector technologies used for IR imaging, two characteristic factors need to be calculated. The first factor is the system responsivity (β), which tells how much current the system can output with a given incident optical power. By using β the second characteristic factor,

Table 10.1 Estimate of the system responsivity (β) for an metal–insulator–metal (MIM) and geometric diode at 28 THz

Diode type	R_D (Ω)	C_D (F)	R_A (Ω)	η_c	β_i (A/W)	β (A/W)
MIM (Ni–NiO–Ni)	50	1.8×10^{-15}	100	0.0079	4.8	0.0379
Geometric diode	200	3.4×10^{-17}	200	0.71	0.3	0.2

Diode responsivity (β_i) is obtained from simulations for MIM diode and geometric diode. We choose diode resistance (R_D) values of 50 Ω for MIM diode and 200 Ω for geometric diode, respectively, because those values gave the highest coupling efficiency with their diode capacitance (C_D), which is fixed for a given device geometry

normalized detectivity (D^*) [25] can be calculated. We calculate these parameters using estimated values for diode geometry parameters and simulated $I(V)$ characteristics.

We assume that β accounts for a product of an antenna absorption efficiency (assumed to be 100 %), an antenna to diode coupling efficiency (η_c), and a current responsivity of the diode (β_i). The β of detectors using an MIM diode and a geometric diode is shown in Table 10.1 [5], for an operating frequency of 28 THz. To estimate the capacitance of the MIM diode, a relative dielectric constant of 12 is used for NiO. The resistance and diode responsivity values are calculated from the simulated DC $I(V)$ curves at 0.38 V bias, which gives the maximum system responsivity of 0.038 A/W. The geometric diode in theory can match the antenna resistance well at 0 V bias and provide diode responsivity of 0.2 A/W. The β of the geometric diode is higher due to a lower capacitance and a better impedance matching with antenna at 28 THz.

The D^* is a measure of the noise performance of the detector and is defined as

$$D^* = (A_d \Delta f)^{1/2} \frac{\beta}{I_n} \quad (1)$$

where

$$I_n = \sqrt{\left(2qI_{ph} + \frac{4KT}{R_D}\right) \Delta f} \quad (2)$$

For the rectenna system, Δf is the bandwidth of the detector and A_d is the area of the detector which equals to the effective area of the antenna. At 28 THz, A_d is 37.5 μm^2 [16]. The noise current (I_n) is calculated as the sum of the shot noise from the diode DC bias current and the Johnson noise from the diode resistance [25]. In all the detectivity analysis, temperature (T) is assumed to be at room temperature (300 K).

Assuming operating at maximum responsivity point (0.38 V bias voltage with 1.48 mA current) and using the data in Table 10.1, the D^* of Ni–NiO–Ni MIM diode at 28 THz is 8.9×10^5 cm $\text{Hz}^{1/2} \text{W}^{-1}$, while the D^* of the geometric diode is 1.7×10^7 cm $\text{Hz}^{1/2} \text{W}^{-1}$. An order of magnitude better performance of the geometric diode is due to its lower RC time constant.

If the operating frequency is lowered to 1 THz, the performance of geometric diode rectenna will be poorer than the MIM diode rectenna. A resistance matched Ni–NiO–Ni MIM rectenna ($100\ \Omega$ at 0.33 V with 0.74 mA bias) will have a coupling efficiency of 0.772 and gives the system responsivity of 5.17 A/W. D^* of MIM at 1 THz will be $1.89 \times 10^8\ \text{cm Hz}^{1/2}\ \text{W}^{-1}$, assuming the antenna area to be $0.09\ \text{mm}^2$. In this case, even assuming the geometric diode has 100 % coupling efficiency, the D^* of the geometric diode is $2 \times 10^7\ \text{cm Hz}^{1/2}\ \text{W}^{-1}$ and still is lower than Ni–NiO–Ni MIM rectenna. Room temperature D^* of both the MIM diode and geometric diode is comparable to the low-temperature performance of other THz detectors [26], and therefore these rectenna detectors have the significant advantage of room temperature operation.

10.11 Summary and Future Work

In summary, we have developed and demonstrated a new kind of diode for use in high-frequency rectennas. The graphene geometric diode exhibits DC $I(V)$ asymmetry caused by diode geometric effect, and its measured electrical characteristics are consistent with Monte Carlo simulations. We have shown that rectennas incorporating geometric diodes rectify $10.6\ \mu\text{m}$ wavelength radiation with both metal and graphene bowtie antennas. The measured short-circuit currents correspond to the values estimated using the diode and antenna parameters. Further improvement in the diode and antenna design is expected to increase rectenna device efficiency. Compared to an MIM diode, a geometric diode has a much higher system responsivity and detectivity at 28 THz because of a lower RC time constant.

Acknowledgements We gratefully acknowledge assistance in device preparation from Kendra Krueger and David Doroski. This work was carried out under a contract from Abengoa Solar, with initial support from Hub Lab. Device processing was carried out in part at the Colorado Nanofabrication Laboratory and in part at the Cornell NanoScale Science and Technology Facility, both members of the National Nanotechnology Infrastructure Network, which is supported by the National Science Foundation (Grant ECS-0335765). We also thank Jonathan Alden in professor P.L. McEuen's group in Cornell University for providing the CVD graphene sample.

References

1. Grover S, Moddel G. Applicability of metal/insulator/metal (MIM) diodes to solar rectennas. *IEEE J Photovolt.* 2011;1(1):78–83.
2. Zhu Z, Grover S, Krueger K, Moddel G. Optical rectenna solar cells using graphene geometric diodes. In: *IEEE photovoltaic specialists conference*; 2011. p. 002120–2.
3. Zhu Z, Joshi S, Grover S, Moddel G. Graphene geometric diodes for terahertz rectennas. *J Phys D Appl Phys.* 2013;46:185101.

4. Moddel G, Zhu Z, Grover S, Joshi S. Ultrahigh speed graphene diode with reversible polarity. *Solid State Commun.* 2012;152:1842–5.
5. Grover S. Diodes for optical rectennas. PhD thesis, University of Colorado, Boulder; 2011. p. 99–101.
6. Datta S. Steady-state transport in mesoscopic systems illuminated by alternating fields. *Phys Rev B.* 1992;45(23):13761–4.
7. Song AM. Electron ratchet effect in semiconductor devices and artificial materials with broken centrosymmetry. *Appl Phys A.* 2002;75:229–35.
8. Ashcroft NW, Mermin ND. *Solid state physics.* New York: Holt, Rinehart and Winston; 1976. p. 2–11.
9. Durkan C. *Current at the nanoscale: an introduction to nanoelectronics.* 1st ed. London: Imperial College Press; 2007. p. 107.
10. Castro Neto AH, Guinea F, Peres NMR, Novoselov KS, Geim AK. The electronic properties of graphene. *Rev Mod Phys.* 2009;81:109–62.
11. Murali Y, Yang Y, Brenner K, Beck T, Meindl JD. Breakdown current density of graphene nanoribbons. *Appl Phys Lett.* 2009;94:243114.
12. Nayfeh OM. Radio-frequency transistors using chemical-vapor-deposited monolayer graphene: performance, doping, and transport effects. *IEEE Trans Electron Devices.* 2011;58(9):2847–53.
13. Joshi P, Romero HE, Neal AT, Toutam VK, Tadigadapa SA. Intrinsic doping and gate hysteresis in graphene field effect devices fabricated on SiO₂ substrates. *J Phys Condens Matter.* 2010;22:334214.
14. Dorgan VE, Bae M-H, Pop E. Mobility and saturation velocity in graphene on SiO₂. *Appl Phys Lett.* 2010;97:082112.
15. Weiss MD, Eliasson BJ, Moddel G. Terahertz device integrated antenna for use in resonant and non-resonant modes and method. Patent No. 6664562; 2003.
16. González FJ, Boreman GD. Comparison of dipole, bowtie, spiral and log-periodic IR antennas. *Infrared Phys Technol.* 2005;46(5):418–28.
17. Williams JR, DiCarlo L, Marcus CM. Quantum Hall effect in a gate-controlled p-n junction of graphene. *Science.* 2007;317:638–41.
18. Sanchez A, Davis CFJ, Liu KC, Javan A. The MOM tunneling diode: theoretical estimate of its performance at microwave and infrared frequencies. *J Appl Phys.* 1978;49:5270.
19. Dragoman D, Dragoman M. Geometrically induced rectification in two-dimensional ballistic nanodevices. *J Phys D Appl Phys.* 2013;46:055306.
20. Vendik OG, Zubko SP, Nikol'skii MA. Modeling and calculation of the capacitance of a planar capacitor containing a ferroelectric thin film. *Tech Phys.* 1999;44(4):349–55.
21. Datta S. Nanoscale device modeling: the Green's function method. *Superlattices Microstruct.* 2000;28(4):253–78.
22. Datta S. The non-equilibrium Green's function (NEGF) formalism: an elementary introduction. In: *Electron devices meeting, 2002. IEDM'02. International; 2002.*
23. Reich S, Maultzsch J, Thomsen C, Ordejon P. Tight-binding description of graphene. *Phys Rev B.* 2002;66:035412.
24. Wu Y, Childs PA. Conductance of graphene nanoribbon junctions and the tight binding model. *Nanoscale Res Lett.* 2011;6(62):1–5.
25. Rogalski A. Infrared detectors: status and trends. *Prog Quant Electron.* 2003;27(2–3):59–210.
26. Rogalski A. *Infrared detectors.* Amsterdam: Goddon and Breach Science Publishers; 2000. p. 776–840.